PAPER

Check for updates

Regulating the coordination geometry of polyhedra in zero-dimensional metal halides for tunable emission†

Zhipeng Zhang,‡ Jin-Feng Liao*‡ and Guichuan Xing ![ORCID] *

Although self-trapped exciton (STE) emissions in zero-dimensional metal halides have been intensively investigated, the understanding of the relationship between the coordination geometries of the metal halides and their photophysical properties is still lacking. In this work, we successfully synthesized single crystals, with strong STE emissions, of the bimetallic materials $(Bmpip)_9[Pb_3Br_{11}](ZnBr_4)_2$ (PbZn-Br) and $(Bmpip)_9[Pb_3Br_{11}](MnBr_4)_2$ (PbMn-Br), where $Bmpip^+$ is 1-butyl-1-methyl-piperidinium ($C_{10}H_{22}N^+$), *via* a facile anti-solvent crystallization strategy. With respect to the monometallic material, $(Bmpip)_2[PbBr_4]$ (Pb-Br), the introduction of Zn^{2+} and Mn^{2+} effectively alters the coordination geometry of the lead bromide polyhedral configuration from a $PbBr_4^{2-}$ tetrahedron to a $Pb_3Br_{11}^{5-}$ trimer. As a result, the maximum emission peak of PbZn-Br exhibits an obvious red shift and the full width at half maximum is almost two-fold wider than that of Pb-Br due to stronger electron–phonon coupling. Moreover, due to the intrinsic emission of the Mn^{2+} ions, an intriguing tunable emission was achieved in PbMn-Br with an impressively high photoluminescence quantum yield of up to 67%. The ultra-stable PbMn-Br single crystals show potential as an ideal down-conversion phosphor for use in UV-pumped white light-emitting diode devices.

Introduction

Tunable luminescent materials that are highly stable and easily prepared are highly desirable for their extensive applications in lighting, display technologies, and bioimaging.[1–6] During the past decade, organic–inorganic hybrid metal halides have garnered particular attention due to their excellent performance not only in photovoltaics but also in the field of light emission.[7–9] By rationally altering the organic cations, the dimensions of the metal halides can be easily controlled at the molecular level, from three dimensions (3D) to two dimensions (2D), one dimension (1D) and even zero dimensions (0D).[10–13] Compared to 3D structures, the soft crystal lattices of low-dimensional structures facilitate the self-trapping of excitons in photoinduced transient lattice defects due to strong phonon–exciton interactions, thus leading to large Stokes shifts and broad luminescence during the relaxation process.[14–16] In 2014, Karunadasa *et al.* reported an intriguing broad emission in a lead halide material, (N-MEDA)PbBr$_4$ (N-MEDA: *N*1-methyl-

ethane-1,2-diammonium). This emission arises from the radiative recombination of self-trapped excitons (STEs).[17] Following this report, tremendous efforts have been devoted to the exploration of STE emissive metal halide materials.[18–20]

0D structures are low-dimensional analogs that enable all single metal halide unit cells to be completely isolated from each other by large organic cations, and thus these structures show the intrinsic emissions of individual metal halide species without mutual interference.[14,21] It is also noteworthy that the intense quantum confinement effect in 0D organic metal halides significantly boosts the photoluminescence quantum yield (PLQY) with respect to 3D, 2D and 1D systems.[15,22] With great efforts devoted to the experimental and theoretical study of 0D materials in recent years, many 0D luminescent metal halides with different geometries (*e.g.*, octahedral SnX_6^{2-}, pyramidal SbX_5^{2-}, and disphenoidal SnX_4^{2-}) have been developed with nearly 100% PLQY.[23–25] Nevertheless, the emissions of these monometallic compounds is typically monochromatic and nonadjustable as they only possess a single acting luminescent species. Moreover, although the effect of metal cations and halide anions on the emission properties have been well studied, a deep in-depth investigation on the relationship between coordination geometries and photophysical properties is still lacking.[26,27]

In this work, we successfully prepared single crystals of a 0D monometallic material, $(Bmpip)_2[PbBr_4]$, and the bimetallic materials, $(Bmpip)_9[Pb_3Br_{11}](ZnBr_4)_2$ and $(Bmpip)_9[Pb_3Br_{11}]$

*Joint Key Laboratory of the Ministry of Education, Institute of Applied Physics and Materials Engineering, University of Macau, Macau, 999078 P. R. China.
E-mail: gcxing@um.edu.mo, jinfengliao@um.edu.mo*
†Electronic supplementary information (ESI) available. CCDC 2238975–2238977. For ESI and crystallographic data in CIF or other electronic format see DOI: https://doi.org/10.1039/d2nr06975j
‡These authors contributed equally to this work.

$(MnBr_4)_2$, where $Bmpip^+$ is 1-butyl-1-methyl-piperidinium $(C_{10}H_{22}N^+)$. A facile anti-solvent crystallization strategy was used and the materials demonstrate strong STE emissions. For simplicity, $(Bmpip)_2[PbBr_4]$, $(Bmpip)_9[Pb_3Br_{11}](ZnBr_4)_2$ and $(Bmpip)_9[Pb_3Br_{11}](MnBr_4)_2$ are denoted as Pb-Br, PbZn-Br and PbMn-Br, respectively. Single-crystal X-ray diffraction (XRD) analysis indicates that alloying lead bromide with Zn^{2+} and Mn^{2+} effectively alters the coordination geometry of the lead bromide cluster from a $PbBr_4^{2-}$ tetrahedron to a $Pb_3Br_{11}^{5-}$ trimer. Comprehensive optical spectroscopy studies reveal that the STE emissions of PbZn-Br and PbMn-Br are largely altered as a result of the geometry changes. It is worth noting that PbMn-Br features two distinct emission centers, the STE-emissive $Pb_3Br_{11}^{5-}$ trimer and the radiative transition of the Mn^{2+} ions, both of which can work independently without mutual energy transfer. As a proof of concept, a white light-emitting diode (WLED) based on the ultra-stable and highly luminescent PbMn-Br was also demonstrated. It is believed that our investigation could provide useful guidance for the mechanistic investigation of STE emissions, inspiring applications in white light illumination as well as anti-counterfeiting.

Results and discussion

As shown in Fig. 1a, single crystals of monometallic Pb-Br and bimetallic PbZn-Br and PbMn-Br were prepared *via* slowly diffusing diethyl ether into a precursor solution containing the metal halide salts and 1-butyl-1-methyl-piperidinium bromide. The Pb-Br and PbZn-Br bulk crystals are colorless

and transparent under ambient light, while the PbMn-Br crystals are light green. The UV-vis absorption spectra of these single crystals are shown in Fig. S1.† Pb-Br and PbZn-Br show negligible visible light absorption, while a distinct absorption peak was observed for PbMn-Br at 450 nm due to the $^6A_1$ to $^4T_1$ transition of the Mn^{2+} ions.[28] Upon excitation with 365 nm UV light, the Pb-Br, PbZn-Br and PbMn-Br crystals exhibit blue, aquamarine and yellow-green emissions, respectively (Fig. 1b). The successful alloying of Zn^{2+} and Mn^{2+} with Pb-Br was verified using scanning electron microscopy-energy dispersive X-ray spectrometry (SEM-EDS). Fig. 1d and e show the homogeneous distribution of elements in the PbZn-Br and PbMn-Br crystals, which confirms the successful alloying of Zn^{2+} and Mn^{2+} with Pb-Br. X-ray photoelectron spectroscopy (XPS) analysis shows the characteristic peaks of the Mn 2p orbitals (645.03 eV and 641.73 eV) and the Zn 2p orbitals (1045.46 and 1022.46 eV) in PbMn-Br and PbZn-Br (Fig. S2 and S3†). To gain further insight into the impact of the Zn^{2+} and Mn^{2+} alloys on the crystal structures, powder XRD patterns were collected (Fig. S4†). The PbZn-Br and PbMn-Br patterns are different from the parental Pb-Br material and display low-angle diffraction peaks ($2\theta < 10°$), suggesting that the Zn^{2+} and Mn^{2+} alloys altered the structure of Pb-Br. To confirm this hypothesis, single-crystal XRD was performed (Fig. S5†). The results reveal that, in contrast to the $PbBr_4^{2-}$ tetrahedron in Pb-Br, the main metal halide species are transformed into $Pb_3Br_{11}^{5-}$ trimers in PbZn-Br and PbMn-Br. In addition, the $ZnBr_4^{2-}$ and $MnBr_4^{2-}$ species form a tetrahedra separated by the organic cations, affording a zero-dimensional metal halide structure. The experimental powder XRD patterns show identical features to
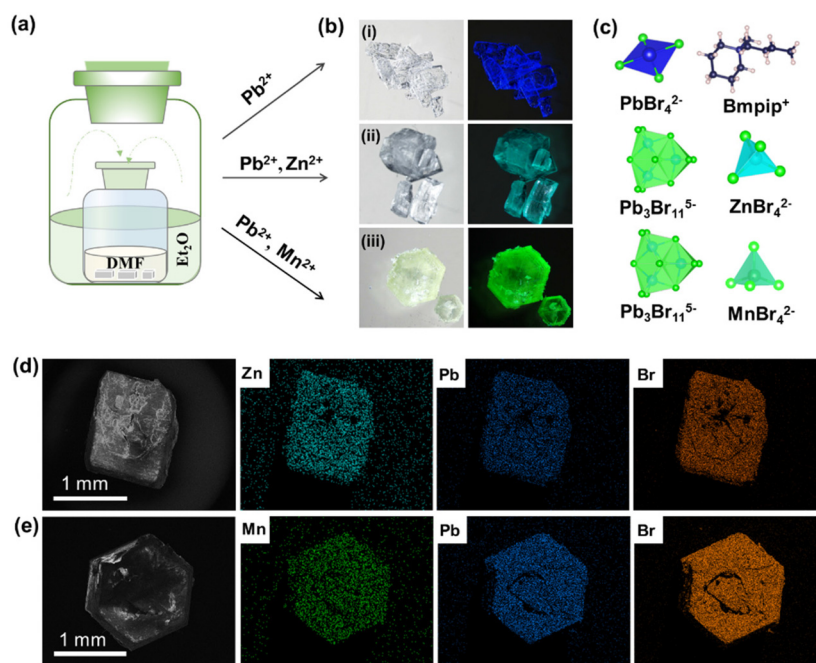

Fig. 1 (a) Scheme for the synthesis of Pb–Br, PbZn–Br and PbMn–Br single crystals. (b) Optical images of Pb–Br (i), PbZn–Br (ii) and PbMn–Br (iii) under ambient light (left) and 365 nm UV light (right). (c) Schematic illustrations of the organic cation and inorganic cluster structures in Pb–Br, PbZn–Br and PbMn–Br. SEM images and the corresponding elemental mapping images of (d) PbZn–Br and (e) PbMn–Br single crystals.

the simulated patterns, confirming the phase purity (Fig. S5d†). Therefore, as shown in Fig. 1c, the introduction of Zn^{2+} and Mn^{2+} into Pb-Br not only brought in new structural units (*i.e.*, $ZnBr_4^{2-}$ and $MnBr_4^{2-}$), but more importantly altered the coordination geometry of the lead bromide from $PbBr_4^{2-}$ to $Pb_3Br_{11}^{5-}$. The crystal structure parameters of these three single crystals are summarized in Table S1 in the ESI.†

As presented in Fig. 2a, the photoluminescence (PL) emission of PbZn-Br when excited at 365 nm exhibits a red-shifted, relative to Pb-Br (470 nm), maximum emission wavelength at 527 nm. In addition, the full width at half maximum of PbZn-Br (114 nm) is almost two-fold wider than that of Pb-Br (65 nm). Consequently, the Commission Internationale de I'Eclairage (CIE) chromaticity coordinates of Pb-Br (0.137, 0.178) was changed to (0.257, 0.456) for the PbZn-Br emission. The emission-wavelength-dependent PL excitation (PLE) spectra of PbZn-Br exhibits the same profile when probed at different emission wavelengths (Fig. 2b). Moreover, the PL spectra of PbZn-Br also exhibit identical features at various excitation wavelengths (340–390 nm). This confirms that there is only one PL center in PbZn-Br, which could be ascribed to the STE emission behavior of the $Pb_3Br_{11}^{5-}$ trimer.[27] The individual $ZnBr_4^{2-}$ tetrahedra and organic cations are photoinactive due to their large band gaps, acting as only building blocks to form the periodically arranged "host" matrix, consistent with other reports.[27,29] Additional accessible experimental evidence for these single exited states is that the emitted photons of different wavelengths display similar photoluminescence lifetimes, close to 38 ns (Fig. 2c). The PL emission intensity linearly increases with the excitation power,

ruling out the possibility of permanent-defects-assisted emission (Fig. S6†), since the intrinsic defect emission is easier to saturate under high excitation power.

On the contrary, two different sets of PL profiles have been characterized in PbMn-Br at different excitation wavelengths (Fig. 2d). A broad emission band peaking at 534 nm with a full width at half maximum (FWHM) of 84 nm was characterized upon excitation with short wavelength light ($320 \leq \lambda_{ex} \leq 370$ nm), while the maximum emission peak shifted to 527 nm with a FWHM of 64 nm upon excitation at 450 nm. The CIE chromaticity coordinates vary as the excitation wavelengths change, which also strongly suggests the existence of more than one emitting center in PbMn-Br (Fig. S7†). To verify this hypothesis, the PLE spectra were collected *via* selectively probing the emitting photons with wavelengths ranging from 460 nm to 600 nm (Fig. 2e). The photons ranging from 460 nm to 485 nm exhibit a maximum excitation wavelength at 393 nm, while the photons with longer wavelengths, from 500 nm to 600 nm, can be easily excited at 453 nm. This strongly indicates two emitting excited states in PbMn-Br, where one is assigned to the STE states in the $Pb_3Br_{11}^{5-}$ trimer and the other is ascribed to the spin-forbidden $^4T_1 \rightarrow {}^6A_1$ transition of the Mn^{2+} ions in $MnBr_4^{2-}$. The Mn^{2+} ion emission is a direct transition process while the emission of the $Pb_3Br_{11}^{5-}$ cluster arises from the STE, which is an indirect emission process. The STE emission originates from the soft crystal lattice and strong electron–phonon interactions, and thus has a typical broad asymmetrical emission band and large Stokes shift. A room-temperature time-resolved PL plot further confirmed the above conclusion. As shown in Fig. 2f, the collected
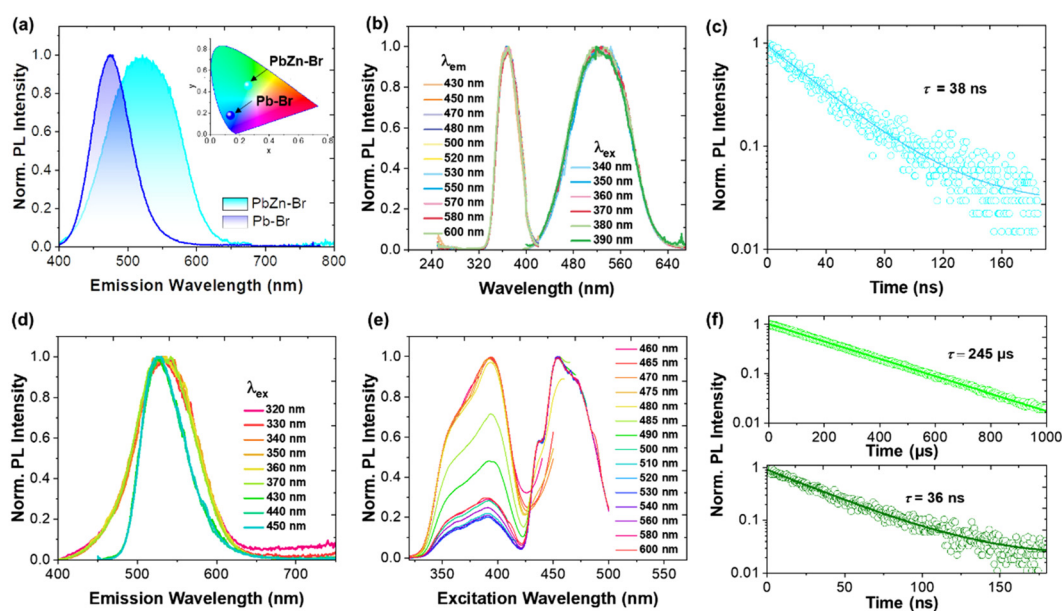
Fig. 2 (a) PL emissions of Pb-Br and PbZn-Br under excitation at 365 nm and their corresponding CIE chromaticity coordinates. (b) Excitation-wavelength dependent emission spectra and emission-wavelength dependent excitation spectra of PbZn-Br. (c) Time-resolved PL emission decay of PbZn-Br. (d) Excitation-wavelength dependent emission spectra of PbMn-Br. (e) Emission-wavelength dependent excitation spectra of PbMn-Br. (f) Time-resolved PL emission decay of PbMn-Br under excitation at 450 nm (top) and 340 nm (bottom).

PL decay curves at 530 nm under excitation at 340 nm and 450 nm can be fitted with a single exponential with a lifetime of 36 ns and 245 μs, respectively. A short lifetime on the nanosecond scale is consistent with the STE emission in the abovementioned PbZn-Br, and a microsecond long lifetime conforms well with Mn^{2+} ion luminescence behavior.[30–32] The PLQY of PbMn-Br is 11% and 67% under excitation at 380 nm and 450 nm, respectively (Fig. 3c), indicating that there is a more efficient radiative recombination process in Mn^{2+} than in $Pb_3Br_{11}^{5-}$. To further confirm the role of the $MnBr_4^{2-}$ units in the PbMn-Br emission, a monometallic Mn-based counterpart was synthesized (Fig. S8†). Regardless of the excitation wavelength, the monometallic Mn-based counterpart exhibits a single emission peaking at 528 nm with a FWHM of 63 nm, nearly identical to PbMn-Br when excited at 430 nm. In addition, the emission lifetime of the monometallic Mn-based counterpart was measured to be 240 μs, further confirming the $MnBr_4^{2-}$ cluster in PbMn-Br is an emission source.

In order to investigate the potential underlying mutual interaction between $Pb_3Br_{11}^{5-}$ and $MnBr_4^{2-}$, temperature dependent PL emissions of PbMn-Br were recorded by selectively exciting samples with 365 nm and 430 nm UV light (Fig. 3a and b). When selectively monitoring the STE in $Pb_3Br_{11}^{5-}$ (365 nm), a strong dependence between the PL

FWHM and temperature was observed (Fig. 3d). As the temperature increased, the PL emission peak gradually widened due to the increasingly strong electron–phonon coupling caused by vibration level relaxation.[33,34] By contrast, the FWHM of the $MnBr_4^{2-}$ emission band is relatively insensitive to temperature vibration (Fig. 3e). To quantitatively evaluate the Huang–Rhys factor (S), the emission FWHM at different temperatures was fitted using the following equation:[35]

$$\text{FWHM}(T) = 2.36\sqrt{S} \times \hbar\omega_{\text{phonon}}\left[\coth\left(\frac{\hbar\omega_{\text{phonon}}}{2Tk_B}\right)\right]$$

where ω_{phonon} is the frequency of the longitudinal optical phonon, $\hbar$ is the reduced Planck constant, T represents temperature (K), and k_B is the Boltzmann constant. As can be seen in Fig. 3f, the S value was calculated to be 33.8 when the $Pb_3Br_{11}^{5-}$ trimers were excited at 365 nm, which is nearly six times larger than that of the $MnBr_4^{2-}$ tetrahedra (5.7) when excited at 430 nm. The S value in the $Pb_3Br_{11}^{5-}$ trimers is also significantly larger than that of most reported traditional semiconductors, such as $CsPbBr_3$ ($S = 3.2$), indicating the strong electron–phonon coupling in our zero-dimensional PbMn-Br systems.[36] The strong electron–phonon coupling is pronounced in the soft lattice of low-dimensional structures and promotes STE formation. In addition, the exciton self-trapping
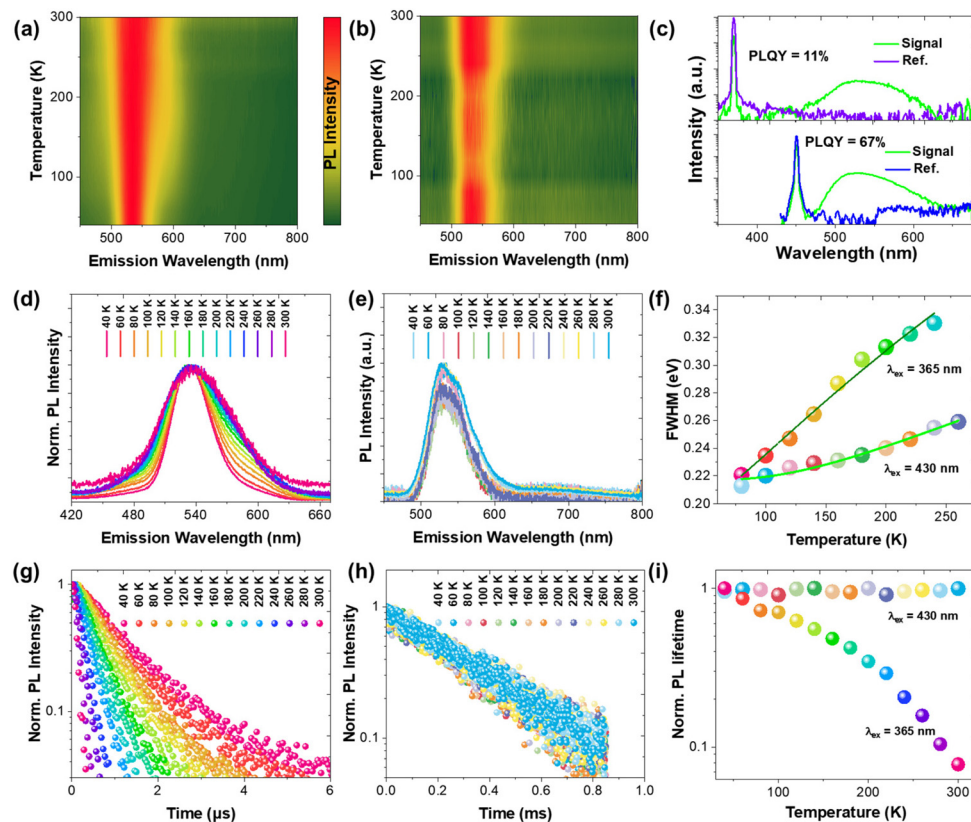
Fig. 3 Temperature-dependent PL emission contour maps of PbMn-Br under excitation at 365 nm (a) and 430 nm (b). (c) PLQY tests of PbMn-Br under excitation at 380 nm (top) and 450 nm (bottom). Temperature-dependent emission spectra of PbZn-Br under excitation at (d) 365 nm and (e) 430 nm, respectively. (f) Plot of PL FWHM *versus* temperature. Temperature-dependent time-resolved PL emission decay of PbMn-Br under excitation at (g) 365 nm and (h) 430 nm, respectively. (i) Plot of PL lifetime *versus* temperature.

time τ of the $Pb_3Br_{11}^{5-}$ trimers was estimated to be 307 fs according to the equation $\tau = 2\pi/\omega_{phonon}$,[37] indicating photoexcitation induces an ultrafast transition from a free exciton to an STE state. Furthermore, the temperature-dependent PL emission decay of the $Pb_3Br_{11}^{5-}$ trimers and $MnBr_4^{2-}$ was measured from 40 to 300 K (Fig. 3g and h). As the temperature increases, the PL lifetime of the $Pb_3Br_{11}^{5-}$ trimers is significantly shortened, probably due to the gradual increase in strength of the electron–phonon interactions (Fig. 3i). By contrast, the PL lifetime of $MnBr_4^{2-}$ is relatively insensitive to temperature variations. The emission intensity grows linearly with the increasing excitation laser power (Fig. S9a–c†), indicating that the emission arises from exciton recombination rather than intrinsic defects.[38,39] Through fitting the data with a power-law equation, a power exponent of $k = 1.0$ was obtained, indicating that the $Pb_3Br_{11}^{5-}$ trimers have intrinsic STE features(Fig. S9d†).[40,41]

Combining the above results, the excited state dynamics and emission mechanism of Pb-Br, PbZn-Br and PbMn-Br can be described (Fig. 4). Upon excitation, electron–hole pairs will be created, and then rapidly interact with a deformable lattice, yielding self-trapped excitons. The self-trapped excitons will then undergo radiative transition from the self-trapped state down to the ground state to emit photons. In the case of PbMn-Br with two emissive centers, precise control of the excitation wavelength could result in a dynamic population distribution in these two independent emitting states, thus leading to dynamic tunable luminescence. Specifically, the $MnBr_4^{2-}$ species does not compete to harvest the high energy photons, probably due to its relatively low light extinction coefficient, and thus in this case the $Pb_3Br_{11}^{5-}$ cluster emission is predominant. While under the excitation of low energy photons ($\lambda_{ex} > 420$ nm), the $Pb_3Br_{11}^{5-}$ cluster is inactive and the $MnBr_4^{2-}$ species will come into play. In contrast to conventional Mn-doped 3D metal halide perovskites where photogenerated free excitons can efficiently transfer to Mn^{2+} ions, no energy transfer was observed between the $Pb_3Br_{11}^{5-}$ and $MnBr_4^{2-}$ clusters in PbMn-Br, probably due to the indirect nature of the STEs.

Some multi-ionic metal halides have been reported recently, and a comparison of their properties is summarized in Table S2.† Dual emissions can generally be achieved in Sn^{2+}-based multi-ionic metal halides.[14,42] However, as we know, Sn^{2+}-based multi-ionic metal halides are susceptible to the rapid oxidation of Sn^{2+} to Sn^{4+}. The stability of multi-ionic metal halides is important for their potential applications in

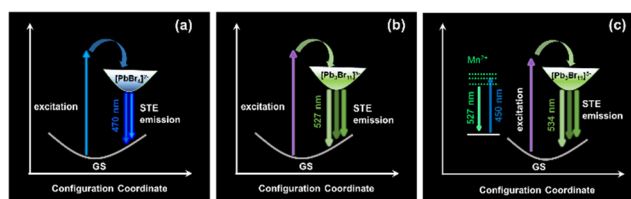light-emitting diodes or anti-counterfeiting. In this work, PbMn-Br exhibits a dual emission and at the same time maintains excellent stability in air and at high temperatures. As shown in Fig. S10,† the powder XRD pattern was still well-preserved when stored in air for about one year (30% relative humidity). In addition, PbMn-Br also exhibited exemplary thermal stability. As shown in Fig. 5a, c and S11a,† greater than 93% of the initial PL intensity remained after continuous heating at 80 °C for 180 min. In contrast, 35% of the initial value was maintained for a green emissive $CsPbBr_3$ nanocrystal due to thermal-induced particle aggregation (Fig. 5b, c and S11b†).[43,44] The PL spectra collected following excitation at 450 nm also demonstrated that the $MnBr_4^{2-}$ species was also undamaged, indicating that these two emissive centers in PbMn-Br have strong thermal resistance (Fig. S12†). The thermogravimetric analysis (TGA) curve indicates that PbMn-Br stays stable even at 250 °C, implying that it has good thermal stability (Fig. 5d). The superior stability of PbMn-Br is because the emissive inorganic polyhedrons are well protected by the bulky organic cations in the zero-dimensional structure.[45] The TGA curves of Pb-Br and PbZn-Br have also been collected and are shown in Fig. S13.† Similar to PbMn-Br, both Pb-Br and PbZn-Br exhibit superior thermal stability without decomposition until 210 °C.

Remarkably, PbMn-Br single crystals not only exhibit high PLQY, but also impressive stability, both of which are required for lighting applications. To demonstrate the above properties, we fabricated a WLED device by mixing PbMn-Br with a commercial phosphor of red $(Sr,Ca)AlSiN_3$:Eu and then exciting the mixture with a 460 nm blue chip. As presented in Fig. 6a, the WLED showed efficient warm white light with the relevant color coordinates at (0.330, 0.313) and a correlated color temperature (CCT) of 5632 K. Furthermore, the as-fabricated device showed remarkable color stability under different driving cur-
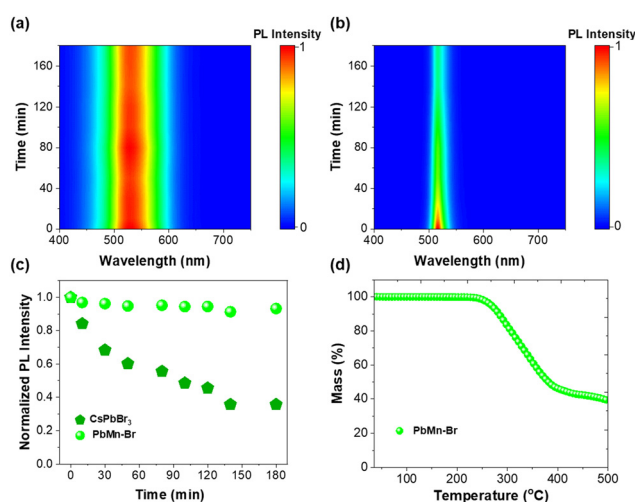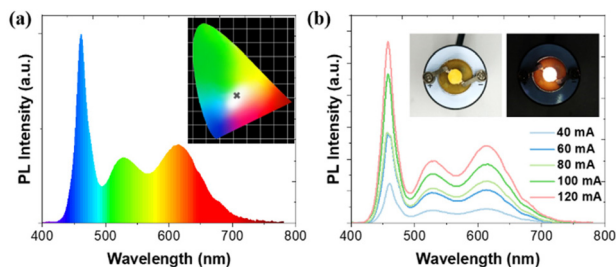

Fig. 5 Time-dependent PL emission contour mappings of (a) PbMn-Br and (b) CsPbBr₃ nanocrystal under continuous heating at 80 °C. (c) The variation of emission peak intensity as a function of heating time. (d) TGA analysis of PbMn-Br.

Fig. 4 Illustration of the PL emission processes in (a) Pb-Br, (b) PbZn-Br and (c) PbMn-Br.

Fig. 6 The EL spectra of the white LED fabricated from a PbMn-Br phosphor and commercial red phosphor CaAlSiN$_3$:Eu^{2+} on a blue LED chip (λ = 460 nm) at a 20 mA drive current (inset: the CIE chromaticity coordinates). (b) The EL spectra under various operating currents from 40 to 120 mA (inset: photograph of fabricated WLED).

rents. The electroluminescent spectral profile remained basically unchanged even upon increasing the driving currents to 120 mA, suggesting that the device had good operation stability (Fig. 6b).

Conclusions

In summary, we successfully synthesized single crystals of 0D monometallic Pb-Br and bimetallic PbZn-Br and PbMn-Br with strong STE emissions *via* a facile anti-solvent crystallization strategy. The alloying of Zn^{2+} and Mn^{2+} into the Pb-Br single crystals effectively alters the coordination geometry of lead bromide from PbBr$_4^{2-}$ to Pb$_3$Br$_{11}^{5-}$. As a result, the STE emission FWHM of PbZn-Br is almost two-fold wider than that of Pb-Br due to stronger electron–phonon coupling. Moreover, due to the intrinsic emission of the Mn^{2+} ions, a distinct multiple species emission was achieved in PbMn-Br. Detailed studies reveal that the STE emissions are highly sensitive to temperature variations due to the strong electron–phonon coupling effect in the soft crystal lattice of Pb$_3$Br$_{11}^{5-}$, while the Mn^{2+} emission is relatively insensitive to temperature. Due to its exemplary photoluminescence quantum yield and stability, PbMn-Br show good performance in a stable white light-emitting diode device. This work not only presents a facile method to prepare color-tunable single phase metal halide materials, but also provides new insights into the relationship between the photophysical properties and coordination geometry of metal halide clusters. We believe this work will provide useful guidance for the future development of luminescent 0D metal halide materials.

Experimental section

Synthesis of Pb-Br, PbZn-Br and PbMn-Br single crystals

For the Pb-Br single crystals, 0.4 mmol of lead bromide and 0.8 mmol of 1-butyl-1-methyl-piperidinium bromide were first dissolved in 2 mL of dimethylformamide (DMF) to form a mother liquid. The bulk crystals were precipitated *via* slowly diffusing diethyl ether into the precursor solution at room temperature overnight. For the PbZn-Br or PbMn-Br single

crystals, the synthetic process is similar to that of Pb-Br, but the raw PbBr$_2$ material was replaced by a mixture of PbBr$_2$ and ZnBr$_2$ or MnBr$_2$, respectively.

Synthesis of CsPbBr$_3$ nanocrystals

PbBr$_2$ and CsBr were dissolved in 6 mL of DMF with 0.1 mL of oleyl amine and 0.3 mL of oleic acid to form a precursor solution. After that, 0.5 mL of the precursor solution was quickly added into 10 mL of toluene with stirring. The CsPbBr$_3$ nanocrystals were collected by centrifugation for use in the stability tests.

Characterization

The optical micrographs were obtained using an inverted Nikon Ti epifluorescence microscope. Single crystal X-ray diffraction studies were performed on an Agilent Technologies Gemini A Ultra system with Cu-Kα radiation (λ = 1.54178 Å) at 150(10) K. Powder X-ray diffraction patterns were collected on an X-ray diffractometer (SmartLab Rigaku, Japan) with Cu-Kα radiation (λ = 1.5406 Å). X-ray photoelectron spectroscopy (XPS) were performed using a Thermo-VG Scientific ESCALAB 250 X-ray photoelectron spectrometer. The SEM images and elemental maps were obtained using a scanning electron microscope (SEM, Zeiss SIGMA, USA). Thermogravimetric analysis (TGA) was carried out using a NetzschTG209F3 TGA system. UV-vis absorption spectra were obtained using an ultraviolet-visible spectrophotometer (V-770, Jasco, Japan). The room-temperature, low-temperature and power-dependent PL spectra were measured on a fluorescence spectrophotometer (SP-2300, Princeton Instruments, USA). Time-resolved PL spectra were measured on a streak camera system (C10910, HAMAMATSU, Japan).

Author contributions

Zhipeng Zhang conducted the measurements and analysed the data. Jin-Feng Liao synthesized the metal halide single crystals. Guichuan Xing conceived the idea. All authors contributed to writing this manuscript.

Conflicts of interest

There are no conflicts to declare.

Acknowledgements

References

1 G. Pacchioni, *Nat. Rev. Mater.*, 2021, **6**, 108–108.

2 Y.-H. Kim, S. Kim, A. Kakekhani, J. Park, J. Park, Y.-H. Lee, H. Xu, S. Nagane, R. B. Wexler, D.-H. Kim, S. H. Jo, L. Martínez-Sarti, P. Tan, A. Sadhanala, G.-S. Park, Y.-W. Kim, B. Hu, H. J. Bolink, S. Yoo, R. H. Friend, A. M. Rappe and T.-W. Lee, *Nat. Photonics*, 2021, **15**, 148–155.

3 S. Li, D. Lei, W. Ren, X. Guo, S. Wu, Y. Zhu, A. L. Rogach, M. Chhowalla and A. K. Y. Jen, *Nat. Commun.*, 2020, **11**, 1192.

4 J. Yin, Y. Yu, X. Song, Y. Jiang and H. Fei, *CCS Chem.*, 2022, **4**, 540–547.

5 J. Chen, Y. Guo, B. Chen, W. Zheng and F. Wang, *J. Am. Chem. Soc.*, 2022, **144**, 22295–22301.

6 L. Gong, F. Huang, Z. Zhang, Y. Zhong, J. Jin, K.-z. Du and X. Huang, *Chem. Eng. J.*, 2021, **424**, 130544.

7 J. J. Yoo, G. Seo, M. R. Chua, T. G. Park, Y. Lu, F. Rotermund, Y.-K. Kim, C. S. Moon, N. J. Jeon, J.-P. Correa-Baena, V. Bulović, S. S. Shin, M. G. Bawendi and J. Seo, *Nature*, 2021, **590**, 587–593.

8 J. Jeong, M. Kim, J. Seo, H. Lu, P. Ahlawat, A. Mishra, Y. Yang, M. A. Hope, F. T. Eickemeyer, M. Kim, Y. J. Yoon, I. W. Choi, B. P. Darwich, S. J. Choi, Y. Jo, J. H. Lee, B. Walker, S. M. Zakeeruddin, L. Emsley, U. Rothlisberger, A. Hagfeldt, D. S. Kim, M. Grätzel and J. Y. Kim, *Nature*, 2021, **592**, 381–385.

9 D. Ma, K. Lin, Y. Dong, H. Choubisa, A. H. Proppe, D. Wu, Y.-K. Wang, B. Chen, P. Li, J. Z. Fan, F. Yuan, A. Johnston, Y. Liu, Y. Kang, Z.-H. Lu, Z. Wei and E. H. Sargent, *Nature*, 2021, **599**, 594–598.

10 S. Paul, K. Ariga, D. D. Sarma and S. Acharya, *Nano Today*, 2021, **39**, 101181.

11 Z. Zhang, S. Wang, X. Liu, Y. Chen, C. Su, Z. Tang, Y. Li and G. Xing, *Small Methods*, 2021, **5**, 2000937.

12 Y. Guo, B. Chen, X. Ren and F. Wang, *ChemPlusChem*, 2021, **86**, 1577–1585.

13 D. Han, H. Shi, W. Ming, C. Zhou, B. Ma, B. Saparov, Y.-Z. Ma, S. Chen and M.-H. Du, *J. Mater. Chem. C*, 2018, **6**, 6398–6405.

14 J.-F. Liao, Z. Zhang, J.-H. Wei, Z.-Z. Zhang, B. Wang, L. Zhou, G. Xing, Z. Tang and D.-B. Kuang, *Adv. Opt. Mater.*, 2022, **10**, 2102426.

15 S. Li, J. Luo, J. Liu and J. Tang, *J. Phys. Chem. Lett.*, 2019, **10**, 1999–2007.

16 B. Chen, Y. Guo, Y. Wang, Z. Liu, Q. Wei, S. Wang, A. L. Rogach, G. Xing, P. Shi and F. Wang, *J. Am. Chem. Soc.*, 2021, **143**, 17599–17606.

17 E. R. Dohner, E. T. Hoke and H. I. Karunadasa, *J. Am. Chem. Soc.*, 2014, **136**, 1718–1721.

18 J.-H. Wei, J.-F. Liao, L. Zhou, J.-B. Luo, X.-D. Wang and D.-B. Kuang, *Sci. Adv.*, 2021, **7**, eabg3989.

19 M. Li and Z. Xia, *Chem. Soc. Rev.*, 2021, **50**, 2626–2662.

20 B. Su, S. Geng, Z. Xiao and Z. Xia, *Angew. Chem., Int. Ed.*, 2022, **61**, e202208881.

21 S. Sun, M. Lu, X. Gao, Z. Shi, X. Bai, W. W. Yu and Y. Zhang, *Adv. Sci.*, 2021, **8**, 2102689.

22 Q. Guo, X. Zhao, B. Song, J. Luo and J. Tang, *Adv. Mater.*, 2022, **34**, 2201008.

23 R. Lin, Q. Zhu, Q. Guo, Y. Zhu, W. Zheng and F. Huang, *J. Phys. Chem. C*, 2020, **124**, 20469–20476.

24 A. Biswas, R. Bakthavatsalam, S. R. Shaikh, A. Shinde, A. Lohar, S. Jena, R. G. Gonnade and J. Kundu, *Chem. Mater.*, 2019, **31**, 2253–2257.

25 J. Luo, M. Hu, G. Niu and J. Tang, *ACS Appl. Mater. Interfaces*, 2019, **11**, 31575–31584.

26 C. Zhou, L.-J. Xu, S. Lee, H. Lin and B. Ma, *Adv. Opt. Mater.*, 2021, **9**, 2001766.

27 S. Lee, C. Zhou, J. Neu, D. Beery, A. Arcidiacono, M. Chaaban, H. Lin, A. Gaiser, B. Chen, T. E. Albrecht-Schmitt, T. Siegrist and B. Ma, *Chem. Mater.*, 2020, **32**, 374–380.

28 B. Su, M. S. Molokeev and Z. Xia, *J. Mater. Chem. C*, 2019, **7**, 11220–11226.

29 M. Li, Y. Li, M. S. Molokeev, J. Zhao, G. Na, L. Zhang and Z. Xia, *Adv. Opt. Mater.*, 2020, **8**, 2000418.

30 M. Li, J. Zhou, G. Zhou, M. S. Molokeev, J. Zhao, V. Morad, M. V. Kovalenko and Z. Xia, *Angew. Chem., Int. Ed.*, 2019, **58**, 18670–18675.

31 Z.-Z. Zhang, J.-H. Wei, J.-B. Luo, X.-D. Wang, Z.-L. He and D.-B. Kuang, *ACS Appl. Mater. Interfaces*, 2022, **14**, 47913–47921.

32 M. Li, J. Zhou, M. S. Molokeev, X. Jiang, Z. Lin, J. Zhao and Z. Xia, *Inorg. Chem.*, 2019, **58**, 13464–13470.

33 R. Saran, A. Heuer-Jungemann, A. G. Kanaras and R. J. Curry, *Adv. Opt. Mater.*, 2017, **5**, 1700231.

34 S. Gong, R. Wu, Q. Han, D. Kong and W. Wu, *J. Mater. Chem. C*, 2022, **10**, 13217–13224.

35 L. Wang, W. Zheng, F. Vitale, X. Zhang, X. Li, Y. Ji, Z. Liu, O. Ghaebi, C. T. Plass, R. Domes, T. Frosch, G. Soavi, E. Wendler, Y. Zhang and C. Ronning, *Adv. Funct. Mater.*, 2022, **32**, 2111338.

36 Y.-C. Peng, S.-H. Zhou, J.-C. Jin, T.-H. Zhuang, L.-K. Gong, H.-W. Lin, Z.-P. Wang, K.-Z. Du and X.-Y. Huang, *J. Phys. Chem. C*, 2022, **126**, 17381–17389.

37 K. Zheng, B. Chen, L. Xie, X. Li, B. Lu, M. Wang, Y. Wu, T. Jiang, F. Zhang, X. Li and Y. Wang, *Adv. Opt. Mater.*, 2022, **10**, 2101661.

38 J. Luo, X. Wang, S. Li, J. Liu, Y. Guo, G. Niu, L. Yao, Y. Fu, L. Gao, Q. Dong, C. Zhao, M. Leng, F. Ma, W. Liang, L. Wang, S. Jin, J. Han, L. Zhang, J. Etheridge, J. Wang, Y. Yan, E. H. Sargent and J. Tang, *Nature*, 2018, **563**, 541–545.

39 Y. Zhang, F. Wang, X. Feng, Z. Zhang, K. Liu, F. Xia, W. Liang, X. Hu, Y. Ma, H. Li, G. Xing and T. Zhai, *Adv. Funct. Mater.*, 2022, **32**, 2205757.

40 H.-L. Xuan, J.-L. Li, L.-J. Xu, D.-S. Zheng and Z.-N. Chen, *Adv. Opt. Mater.*, 2022, **10**, 2200591.

41 Q. Li, B. Xu, Z. Chen, J. Han, L. Tan, Z. Luo, P. Shen and Z. Quan, *Adv. Funct. Mater.*, 2021, **31**, 2104923.

42 L.-J. Xu, S. Lee, X. Lin, L. Ledbetter, M. Worku, H. Lin, C. Zhou, H. Liu, A. Plaviak and B. Ma, *Angew. Chem., Int. Ed.*, 2020, **59**, 14120–14123.

43 M. Liu, Q. Wan, H. Wang, F. Carulli, X. Sun, W. Zheng, L. Kong, Q. Zhang, C. Zhang, Q. Zhang, S. Brovelli and L. Li, *Nat. Photonics*, 2021, **15**, 379–385.

44 J.-F. Liao, Y.-F. Xu, X.-D. Wang, H.-Y. Chen and D.-B. Kuang, *ACS Appl. Mater. Interfaces*, 2018, **10**, 42301–42309.

45 H. Peng, Y. Tian, Z. Yu, X. Wang, B. Ke, Y. Zhao, T. Dong, J. Wang and B. Zou, *Sci. China Mater.*, 2022, **65**, 1594–1600.